Journal of Materials Chemistry C

ROYAL SOCIETY OF CHEMISTRY

PAPER

View Article Online
View Journal

Cite this: DOI: 10.1039/d5tc03467a

The key role of soft corona in the superlattice formation of CeO_2 nanoparticles

Noemi Gallucci,[ab] Alessandro Cangiano,[ab] Rosario Oliva,[a] Donato Ciccarelli,[ab] Gennaro Rollo,[c] Rocco Di Girolamo,[a] Nathan Cowieson,[d] Giuseppe Vitiello[be] and Luigi Paduano[*ab]

Received 17th September 2025,
Accepted 8th February 2026

DOI: 10.1039/d5tc03467a

rsc.li/materials-c

The fabrication of superlattices is nontrivial because nanoparticles are notoriously difficult to employ due to the complex nanoscale forces among them. An effective way to manipulate these nanoscale forces is to use a soft corona around the solid core. The soft corona can be engineered to alter the forces between nanoparticles—either attracting or repelling them, and thereby influence their self-assembly process. Here, a deep analysis is proposed on how amines of different lengths (C8 to C18) can influence the hierarchical superlattice organization of cerium oxide nanoparticles, from both structural and energetic perspectives, and the consequent optical properties. The aim is to demonstrate how it is possible to shift from disordered to ordered aggregates and how to obtain one structure instead of another by modulating the geometrical and energetic parameters of soft corona/solid core nanoparticles. The results show that organic coating plays a key role in the self-aggregation process of superlattices with advanced optical properties, thereby broadening the range of potential applications for nanoparticles.

1. Introduction

Cerium oxide nanoparticles (CeO_2 NPs) are gaining considerable attention in various scientific and industrial fields due to their unique physicochemical properties. As the most abundant rare earth element in the Earth's crust, cerium forms nanoparticles that exhibit a remarkable ability to undergo continuous redox cycling between the Ce^{3+} and Ce^{4+} oxidation states.[1] This redox flexibility, coupled with high oxygen mobility[2,3] and a long luminescence lifetime of charge carriers, positions CeO_2 NPs as excellent candidates for photocatalytic applications, particularly under UV light. Their wide bandgap (3.0–3.4 eV) enhances their photocatalytic efficiency, making them comparable to, and in some cases superior to, titanium dioxide nanoparticles (TiO_2 NPs).[4,5] Beyond photocatalysis, CeO_2 NPs show significant promise in biomedicine, where their tunable redox properties can either mitigate oxidative stress through antioxidant activity or promote it for therapeutic purposes such as cancer treatment.[6–9] Additionally, their enzyme-like behavior has led to their classification as "nanozymes", expanding their potential applications in bioimaging, biosensing, and environmental remediation.[8] The properties and thus the applications of these interesting nanoparticles can be further enhanced by inducing an ordered superlattice self-assembly.

Superlattices are structured arrays composed of inorganic nanomaterials, including metals, metal oxides, magnetic nanoparticles, and quantum dots. These assemblies can exhibit remarkable new collective properties that differ from those of individual nanoparticles or their bulk counterparts.[10–12] However, creating nanoparticle superlattices is challenging because nanoparticles are notoriously difficult to manipulate due to the complex forces at the nanoscale. A practical approach to managing these forces is to use soft ligands. These ligands can prevent disordered aggregation of nanoparticles, adjust the interparticle potential, and control lattice structures and interparticle distances, which are the two key factors that determine the properties of superlattices.[13,14]

The soft corona/solid core nanoparticles could lead to a variety of lattice structures, such as face-centered cubic (FCC), body-centered cubic (BCC), hexagonal-close-packed (HCP), diamond-like lattice, and distorted structures, such as Frank-Kasper phases.[15] These different structures can be directly related to the length of the soft ligands, which play a critical role in resulting superlattice properties by controlling interparticle spacing.[13] The space between neighboring nanoparticles, or rather voids, can determine the formation of one type of lattice *versus* another. For example, for hard spheres, considering the

[a] Department of Chemical Sciences, University of Naples Federico II, 80126, Naples, Italy. E-mail: luigi.paduano@unina.it
[b] CSGI, Center for Colloid and Surface Science, 50019, Sesto Fiorentino, Italy
[c] CNR-IPCB Istituto per i Polimeri, Compositi e Biomateriali, 80055, Portici, Italy
[d] Diamond Light Source, Didcot, Oxfordshire, England, UK
[e] Department of Chemical, Materials and Production Engineering, University of Naples Federico II, 80125, Naples, Italy

two structures, FCC and HPC, which have the same degree of occupancy of the lattice (~74%) and a difference in translational entropy per particle that differs by only $0.001k_BT$, the preference of one structure over the other depends on the formation of different voids, namely octahedral voids (OVs) and tetragonal voids (TVs), respectively. OV voids allow more solvent molecules to be incorporated than TV sites, which are preferentially occupied by more ligand molecules.[16] This influences the interaction potentials between neighboring nanoparticles, such as elastic and hydrophobic.[11,14]

Not only does the length of the alkyl chains of the organic coating influence the aggregation of nanoparticles into ordered structures, but so does the density of the soft corona surrounding the inorganic core. Indeed, an optimal number of ligands is generally required to obtain ordered structures, and in some cases, it is necessary to partially remove the coating to promote attractive interactions between the inorganic cores.[13] Moreover, the nature of the organic coating and the process by which the nanoparticle aggregate is formed are of fundamental importance.[17,18] Consequently, this appears as an open question to be investigated.

Given the key role of soft corona, the length of the alkyl chains of the organic coating, and the degree of coating of the solid core, as mentioned above, we aim to investigate how the soft corona affects self-assembly into different structures and, consequently, the properties of the resulting superlattices. For this reason, we have synthesized and characterized CeO_2 NPs coated with primary amines of varying alkyl chain lengths, from C8 to C18. Then, we used oleic acid to promote self-assembly through an emulsion process. In this way, we have been able to modulate the type of superlattice obtained and, consequently, to modulate the emission properties of these 3D systems. The choice of a multi-methodological approach lies in investigating the structural, energetic, and optical properties of these superlattices.

2. Experimental section

2.1 Materials

Cerium(III) nitrate hexahydrate $Ce(NO_3)_3{\cdot}6H_2O$ (>99.999% trace metals basis purity), octylamine $C_8H_{19}N$ (C8, 99% purity), decylamine $C_{10}H_{23}N$ (C10, 95% purity), dodecylamine $C_{12}H_{27}N$ (C12, 98% purity), hexadecylamine $C_{16}H_{35}N$ (C16, 98%, purity), oleylamine $C_{18}H_{37}N$ (C18, 70% technical grade), oleic acid $C_{18}H_{34}O_2$ (OA, ≥99% purity) 1-octadecene (90% technical grade), ethanol (96% vol), chloroform (≥99.5%, contains 100–200 ppm amylenes as a stabilizer) were purchased from Merck (Germany) and used without further purification. All aqueous solutions were prepared using double-distilled Milli-Q water, filtered using 0.20 μm filters, with the only exception of samples for Cryo-TEM and SANS where D_2O (Merck, Italy) was used.

2.2 Synthesis of amine@CeO_2 NPs

Amine@CeO_2 NPs were synthesized through a modified version of the thermal decomposition method introduced by Lee *et al.*[19] and already used in our previous work.[20] Namely, 1.74 g of $Ce(NO_3)_3{\cdot}6H_2O$ were dissolved in 25 mL of 1-octadecene at room temperature. Upon the dissolution of the salt, a specific amount of each selected capping agent was alternatively added to the reaction mixture, as reported in Table S1, to obtain a 1 : 3 salt : capping agent molar ratio. Each resulting solution was placed in a bath at 80 °C and stirred for 30 minutes. Then, the solution was further heated at different temperatures to monitor the effect of thermal conditions, as summarized in Table S1, under an argon atmosphere and stirred for 1 hour. The reaction mixture was then slowly cooled down to room temperature, and 30 mL of ethanol were added to induce the precipitation of NPs. The resulting suspension was transferred into 50 mL centrifuge tubes and centrifuged at 8000 rpm for 20 minutes. Then the supernatant was discarded, and the amine@CeO_2 NPs were re-dispersed in ethanol. The centrifugation step was repeated twice to remove all the unreacted material. Finally, amine@-CeO_2 NPs were dispersed in chloroform.

2.3 Superlattice formation

The micro-emulsion method was selected to induce superlattice formation as previously described.[20,21] Specifically, the interaction between the alkyl chains of the capping agent induced the self-assembly of amine@CeO_2-NPs, which have been made stable in water through the encapsulation of the functionalizing molecules, OA. This last step was preceded by a solvent change. Indeed, the synthesized amine@CeO_2 NPs were centrifuged and recovered in ethyl ether. Then, OA was dissolved in an amine@CeO_2 NPs suspension, and subsequently, 10 mL of bi-distilled water were added to each organic solution to obtain biphasic systems. These systems were sonicated with a probe tip-sonicator for 5 minutes and held under stirring overnight to remove the organic solvent in order to get monophasic systems.[21]

2.4 Morphological characterization

Transmission electron microscopy (TEM) images were acquired to investigate the morphology and the size of the inorganic core of amine@CeO_2 NPs, and the morphology of superlattices using a microscope the FEI TECNAI G2 200 kV (FEI Company, Dawson Creek Drive Hillsboro, Hillsboro, OR USA). Approximately 10 μL of a given sample was placed on a carbon-coated copper grid and allowed to air dry before imaging.[20,22]

Cryogenic transmission electron microscopy (Cryo-TEM) measurements were performed to characterize superlattice structures and to determine the parameters that drive the hierarchical organization. Cryo-TEM images were carried out at Heinz Maier-Leibnitz Source, Garching Forschungzentrum (Germany), on a JEOL 200 kV JEM-FS2200 with a field emission gun (FEG). Samples for Cryo-TEM were prepared by placing a 5 μL drop of superlattice suspension on a Quantifoil Multi A carbon-coated copper grid. After, the sample was cryo-fixed by rapidly immersing it into liquid ethane at −180 °C in a cryo-plunge (EMGP Leica GmbH). The grid was inserted into a cryo-transfer holder (HTTC 910, Gatan, Munich, Germany) and transferred to a JEM 2200 FS EFTEM instrument (JEOL, Tokyo, Japan). Examinations were carried out at a temperature of around −180 °C. The transmission electron

microscope was operated at an acceleration voltage of 200 kV. All images were recorded digitally by a bottom-mounted 16-bit CMOS camera system (TemCam-F2016, TVIPS, Munich, Germany). Images were taken with the EMenu 4.0 image acquisition program (TVIPS, Munich, Germany) and processed with a free digital imaging processing system, ImageJ.[21]

2.5 Dimensional and structural characterization

Dynamic light scattering (DLS) measurements were performed to measure the size of amine@CeO_2 NPs in chloroform with a home-made instrument composed of a Photocor compact goniometer, an SMD 6000 Laser Quantum 50 mW light source (Quantum Laser, Heaton Mersey, UK) operating at 532.5 nm, a photomultiplier (PMT-120-OP/B), and a correlator (Flex02-01D) from Correlator.com. The experiments were carried out at a constant temperature (25.0 ± 0.1) °C, using a thermostatic bath, and at a scattering angle θ of 90°. The diffusion coefficient of the scattered particles, approximated as spherical objects, was used to determine the hydrodynamic radius.[20,22]

Small-angle X-ray scattering (SAXS) measurements were carried out to determine the ordered structures in which the coated CeO_2–NPs were arranged. SAXS analysis was performed at the beamline B21 of the diamond light source (Didcot, UK). The experiments were carried out at 25 °C. The beamline configuration was with a beam energy of 13.1 keV and a sample-to-detector distance of 3.7 m. This configuration allowed us to collect the data for the scattering vector modulus $Q = 4\pi \sin(\theta/2)/\lambda$ in the range of values between 0.0026 $Å^{-1}$ and 0.34 $Å^{-1}$, where θ is the scattering angle.[23]

Small-angle neutron scattering (SANS) analysis was performed to determine the characteristic structural parameters of the superlattice aggregates present in the systems. SANS measurements were carried out at the KWS-1 beamline of the Heinz Maier-Leibnitz Zentrum (Munich, Germany). Structural information was obtained by fitting the experimental data with an appropriate model. In this case, the face-centred cubic lattice was used: $I(q) = \frac{\text{scale}}{V_p} V_{\text{lattice}} P(q) Z(q)$, where $V_{\text{lattice}} = \frac{16\pi}{3} \frac{R^3}{\left(D\sqrt[2]{2}\right)^3}$.

2.6 Organic coating characterization

The presence of the organic coating on the NPs surface was verified by IR spectroscopy. The spectra were collected in the range of 4000–400 cm^{-1} by using an FT-IR 4700 Jasco spectrometer (Milan, Italy).[24]

The quantification of the soft corona was performed through thermogravimetric analysis (TGA). The curves were collected in the temperature range between 50 and 550 °C with a rate of 10 °C min^{-1} by using a Q550 TA Instruments (New Castle, USA), under Nitrogen flow.

2.7 Optical characterization

To investigate the optical properties of the superlattices, fluorescence spectroscopy experiments were carried out. To select the optimal excitation conditions for the samples, absorption measurements were performed prior to the emission ones. UV-visible spectroscopy analysis was performed to determine the absorption properties of superlattices and to prepare the samples so that at the wavelength of excitation, they have the same absorbance. Absorption spectra were recorded in the range 190–600 nm, by using a Jasco V-770.[20] Instead, fluorescence emission spectra were recorded using a Fluoromax-4 spectrofluorometer (Horiba France SAS, JobinYvon, Palaiseau, France) equipped with a Peltier control system (T = 20 °C) and using a 1 cm path length quartz cuvette. The wavelength of excitation was set to 250 nm. Instead, the width slits of both excitation and emission monochromators was set to 7 nm.[21]

3. Results and discussion

Amine-coated cerium oxide nanoparticles (amine@CeO_2 NPs) were successfully synthesized through the thermal decomposition of cerium(III) nitrate hexahydrate with all amines used as capping agents and at all operating temperatures. The results obtained from the characterization (see SI section) of the synthesized NPs demonstrate that the synthesis at 150 °C leads to the formation of NPs aggregates with irregular shapes (Fig. S1 and S2A). This could occur because of $Ce(NO_3)_3{\cdot}6H_2O$ precursor melts at 57 °C but thermally decomposes between 190 and 300 °C, thus causing an inhomogeneous growth of nanoparticles.[25] In contrast, by increasing the synthesis temperature and the length of the alkyl chain of the capping agent, the size of the inorganic core of the single NPs was reduced (Fig. S2), the spherical morphology was favored, while the tendency to self-assembly was strongly reduced (Fig. S1). These experimental results align with those reported by Lee and coworkers.[26] By utilizing the same synthesis procedure and oleylamine as a capping agent, they synthesized CeO_2 NPs with an inorganic core size of approximately 5 nm. They also point out that increasing reaction times is necessary to decrease the polydispersity in the core size, which contrasts with what was observed in this and our previous work.[20] The different synthesis conditions produced a different organic coating density (Fig. S5), which was lower (about 2 chains per nm^2, ~50% surface coverage) for the shorter amines (C10 and C12) and higher (about 5 chains per nm^2, ~99% surface coverage) for the longer amines (C16 and C18), thus influencing the aggregation process and the subsequent self-assembly into ordered superlattices. By changing precursor, solvent, reaction time, temperature, and organic coating, it is possible to have a number of NPs of different shapes, sizes, and properties. Consequently, the amine@CeO_2 NPs synthesized at 200 and 250 °C were selected to be functionalized with oleic acid (OA-amine@CeO_2 NPs).

3.1 OA-amine@CeO_2 NPs: investigating the structure of the superlattices

The superlattices can be described geometrically in terms of a close packing of equal spheres, held together by interatomic forces.[13,17,18]

For this reason, to understand the type of ordered structures that can be induced in coated CeO_2 NPs, the data from the OA-amine@CeO_2 NPs will be analyzed in terms of the length of

the alkyl chain of the capping agent and the size of the inorganic core. In all cases, the functionalization with OA leads to the formation of aggregates in aqueous suspension. The obtained systems were characterized by combining SAXS, cryo-TEM, and TEM techniques. The choice of a multi-methodological approach lies in investigating the structural and morphological properties of these aggregates both in solution and as dry samples.

3.1.1 OA-C10@CeO_2 and OA-C12@CeO_2: formation of disordered structures. The SAXS curve of OA-C10@CeO_2 presents a slope of Q^{-3} (Fig. 1A), typical of disordered NPs aggregates,[27] which are also confirmed from the cryo-TEM image (Fig. 1B). Despite subtracting the form factor of a sphere from this raw data (Fig. S7A), no peaks are detected. In the OA-C12@CeO_2 sample, aggregates with a disordered distribution are visible. When the form factor of a sphere is subtracted from the SAXS data (Fig. S7A), a peak appears at a scattering vector Q value of approximately 0.08 $Å^{-1}$ (Fig. 1C). This corresponds to an average distance between nanoparticles of about 7.8 nm (Table S5), which aligns with the value determined by the statistical analysis of the cryo-TEM image, where $d = 7 \pm 2$ nm, as shown in Fig. 1D.

In both cases, the building blocks are disordered aggregates of amine@CeO_2 NPs. For this reason, no speculation will be made on the geometric and energetic parameters involved.

3.1.2 OA-C16@CeO_2 and OA-C18@CeO_2: formation of ordered structures. The analysis of the SAXS patterns for OA-C16@CeO_2 (Fig. 2A) and OA-C18@CeO_2 (Fig. 3A) shows a repetitive structure factor peak pattern, which is characteristic of ordered structures. Specifically, the spacing and arrangement of these peaks suggest compatibility with both a face-centered cubic phase (FCC) and a hexagonal Frank-Kasper phase (C14 FK). This compatibility is evident when comparing the experimental Q/Q_1 data with similar systems documented in the literature for the two phases, FCC and C14 FK (see Table S2).

The distances between the peaks in the SAXS profile (Fig. 2A) and the analysis of the cryo-TEM image (Fig. 2B, and the corresponding FTT in Fig. 2F) indicate a separation of approximately 7.2 nm between two neighboring NPs. Additionally, the angle between two rows is about 120°. These measurements are more consistent with a C14 FK phase, which has cell parameters of $a = b \sim 8.8$ nm and $c \sim 14.4$ nm.[15,21]

Interestingly, in other areas of the grid analyzed by cryo-TEM, clusters of NPs adopting another ordered arrangement appear. Here, the rows of NPs create angles of approximately 90°, which is characteristic of cubic structures (see Fig. 2C, and corresponding FTT in Fig. 2G). These ordered phases coexist alongside with individual NPs (refer to Fig. 2D). These findings indicate that the OA-C16@CeO_2 sample is highly heterogeneous, featuring both single NPs and various types of ordered structures, likely coexisting with disordered aggregates related to the broad SAXS peaks. The range of spatial order ($\xi = 2\pi/\Delta Q$) was calculated referring to the half-height amplitude (ΔQ) of the most intense peak,[28] and estimated to be about 55 nm.

In the case of OA-C18@CeO_2, the SAXS profile (Fig. 3A) and the analysis of the cryo-TEM images (Fig. 3B) indicate that the distance between two neighboring NPs is approximately 7.9 nm. Additionally, there is an angle of about 90° between the rows of NPs, which aligns more closely with a face-centered cubic (FCC) phase, characterized by cell parameters $a = b = c \approx 1.7$ nm, and also the Fourier transform (Fig. 3C) confirms the FCC phase.[15,21] Nevertheless, the broad peaks of the SAXS data suggest the coexistence of several ordered or even disordered phases. In fact, a similar range of spatial order, approximately 70 nm, is also observed in this case.

For the CeO_2 NPs synthesized at 200 °C and coated with C16 or C18, the combined radius – accounting for both the inorganic

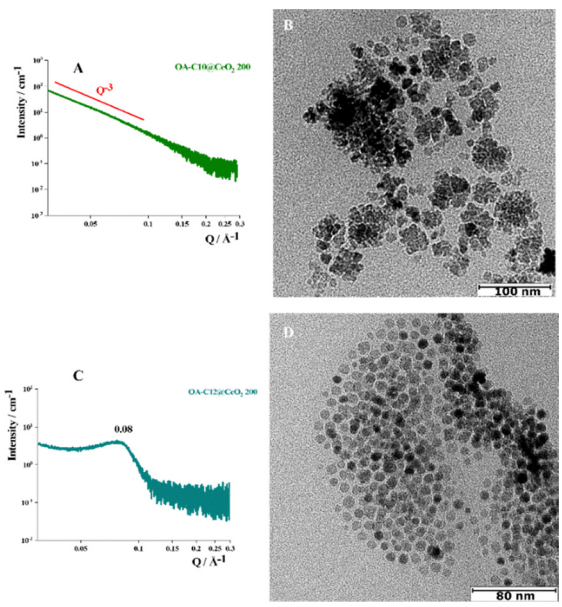

Fig. 1 SAXS pattern of OA-C10@CeO_2 in H_2O (A), cryo-TEM image of OA-C10@CeO_2 in D_2O (scale bar: 100 nm) (B), SAXS pattern of OA-C12@CeO_2 in H_2O (C), and cryo-TEM of OA-C12@CeO_2 in D_2O (scale bar: 80 nm) (D).

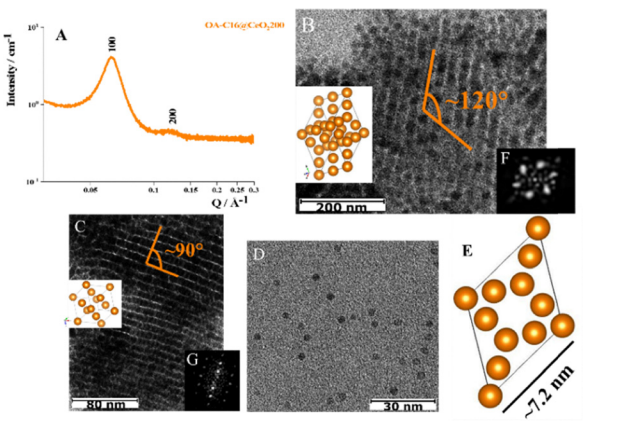

Fig. 2 SAXS pattern in H_2O (A), cryo-TEM image in D_2O with 3D schematic representation of C14 FK (scale bar: 200 nm) (B), cryo-TEM image in D_2O with 3D schematic representation of FCC (scale bar: 80 nm) (C), and cryo-TEM of single nanoparticles in D_2O (scale bar: 30 nm) (D) of OA-C16@CeO_2 200, 2D schematic representation of C14 FK phase with experimental distance between two NPs (E), FTT of cryo-TEM in B (F), and FTT of cryo-TEM in C (G).

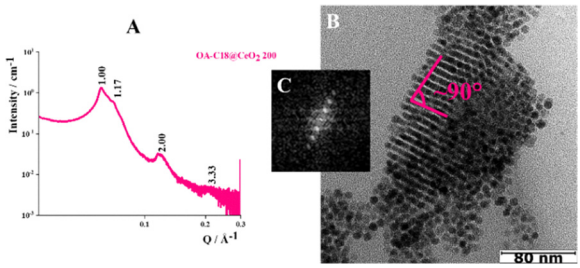

Fig. 3 SAXS pattern in H_2O with 3D schematic representation of FCC phase (A), cryo-TEM in D_2O (scale bar: 80 nm) (B) of OA-C18@CeO_2, and FTT of cryo-TEM in B (C).

core and the length of the capping agents – is approximately 6.6 nm. When this dimension is considered as the radius of a hard sphere within a lattice framework, it implies that the spatial volume occupied by each NPs contributes to the formation of a heterogeneous (composed of ordered, disordered, and single NPs) hierarchical organization.

In the case of the NPs synthesized at 250 °C and coated with C16 amine, the sum between the radius of the inorganic core and the length of the alkyl chains decreases from 6.6 to 5.1 nm ($\langle R \rangle \sim 2.9$ nm, C16 length in its full-length extension ~2.2 nm). The analysis of the SAXS pattern (Fig. 4A) reveals structure factor peaks typical of a hexagonal phase (Table S3). The experimental values of Q/Q_1 align with expectations for a configuration of NPs in the Frank-Kasper phase featuring a hexagonal unit cell (C14 phase). The presence of the hexagonal phase is also confirmed by cryo-TEM images; in particular, Fig. 4C shows the honeycomb structure, typical of FK phases.[15,21,29] Based on the data, the cell parameters have been calculated as follows: $a = b \approx 9.1$ nm and $c \approx 14.9$ nm.

In addition to this C14 Frank-Kasper phase, the presence of single functionalized CeO_2 NPs is detected by TEM analysis (Fig. S8). Nevertheless, ξ is about 56 nm, so probably the reduction of the volume of the sphere reduces the presence

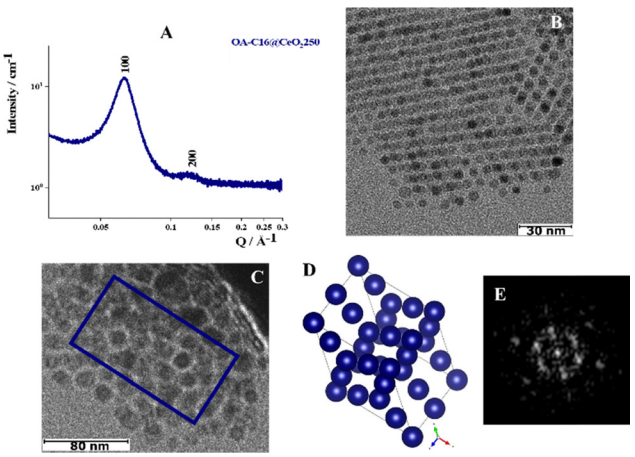

Fig. 4 SAXS patter in H_2O (A), cryo-TEM image of C14 FK phase in D_2O (scale bar: 30 nm) (B), cryo-TEM image of C14 FK phase in D_2O (scale bar: 80 nm) (D) of OA-C16@CeO_2 250, 3D schematic representation of C14 FK phase (D), and FTT of cryo-TEM in B (E).

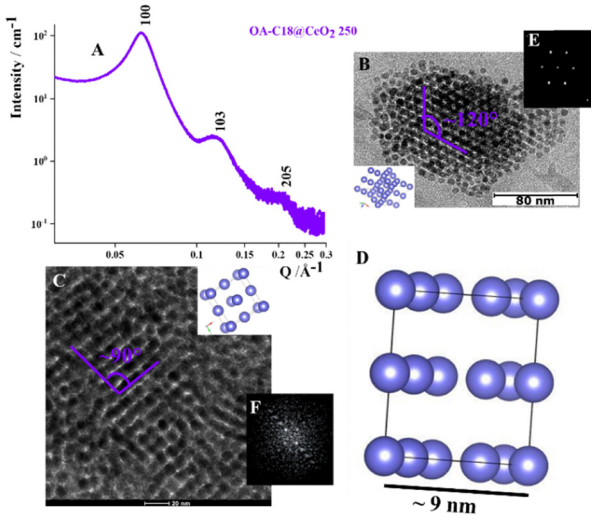

Fig. 5 SAXS pattern in H_2O (A), cryo-TEM image with 3D schematic representation of C14 FK in D_2O (scale bar: 80 nm) (B), and TEM image with 3D schematic representation of FCC (scale bar: 20 nm) (C) of OA-C18@CeO_2 250, 2D schematic representation of C14 FK phase with experimental cell parameters (D), FTT of cryo-TEM in B (E), and FTT of TEM in C (F).[21]

of disordered aggregates but does not increase the extension of the order into the aggregates. Reducing the value from 5.1 to 4.9 nm, considering the OA-C18@CeO_2 system ($\langle R \rangle \sim 2.5$ nm, C16 length in its full-length extension ~2.4 nm), the analysis of SAXS pattern (Fig. 5A) revealed, also in this case, structure factor peaks typical of a hexagonal phase, with the experimental values of Q/Q_1 comparable to that a C14 FK phase (Table S4). In addition, the analysis of cryo-TEM image (Fig. 5B) shows the presence of a distorted compact hexagonal structure with lattice parameters $a = b \sim 9.0$ nm, $c \sim 14.7$ nm, and $\theta \sim 115°$.[21] However, TEM images indicate the formation of an organization of OA-C18@CeO_2 250 NPs with an angle of about 90° between neighboring NPs (Fig. 5C).[21] Also in this case, the extension of the order is about 62 nm. These results indicate that, by reducing the volume occupied by the single NP in the superlattice, it is possible to reduce the presence of both the disordered aggregates and the functionalized single NPs. At the same time, in the OA-C18@CeO_2 system synthesized at 250 °C, the coexistence of several ordered phases, above all C14 FK and FCC ones, is observed, although with a different relative amount.

3.2 OA-amine@CeO_2 NPs: thermodynamic insights into the self-assembly of superlattices

The interactions between inorganic NPs are quite complex, involving various forces at different temporal and spatial scales.[11] Thanks to the combination of experimental, theoretical, and extrapolated data (Table S6), van der Waals, elastic, hydrophobic, osmotic, and total interaction potential between two amine@CeO_2 NPs (OA-C16@CeO_2 200, OA-C18@CeO_2 200, OA-C16@CeO_2 250, and OA-C18@CeO_2 250) have been calculated. In all cases, the osmotic and elastic interactions are negligible to those of van der Waals and hydrophobic (Fig. S9).

Elastic interactions are repulsive interactions that occur due to a loss of configurational entropy of ligand chains when the distance between two nanoparticles is less than the length of the alkyl chain of ligands themselves.[11] These interactions depend mainly on ligand parameters, such as molecular weight, and degree of coating (eqn (S1)). On the other hand, osmotic interactions (eqn (S2)) are interactions between ligands and solvents. It occurs when it is necessary to balance the osmotic pressure between the region between the NPs (few solvent molecules) and those outside the NPs (many solvent molecules).[30] In all the cases, these two interaction potentials are negligible.

The introduction of water into the system at the time of superlattice preparation induces self-assembly due to the presence of hydrophobic interaction potentials (eqn (S3)).[30] The increasing surface tension of the amine in water (γ_{C16} = 3.07 × 10^{-3} mN m^{-1}, γ_{C18} = 3.14 × 10^{-3} mN m^{-1}) increases the hydrophobic interaction in the system. Finally, the van der Waals potentials (eqn (S4)) depend on the dimension of the inorganic core, Hamaker's constant, and the core–core distance. This indicates that as the core–core distance decreases, the potential drops to a minimum at the point where the surfaces of the two NPs come into contact and therefore tends to infinity due to the impossibility of overlapping two spheres.

Although the trends of the different contributions are the same for all the studied samples (Fig. S9), the comparison of the total interaction potentials obtained from the sum of the different contributions indicates clear differences between the four samples (OA-C16@CeO_2 200, OA-C18@CeO_2 200, OA-C16@CeO_2 250, and OA-C18@CeO_2 250) (Fig. 6).

The trend in Fig. 6 shows how geometric parameters, such as the radius of the inorganic core and the length of the alkyl chain of the organic coating, affect the total interaction potential. As the radius of the inorganic core decreases and the length of the alkyl chain increases, the minimum becomes less pronounced and moves to smaller core–core distances. Taking into account that the nanoparticles are almost completely coated, it has been shown that in this case, any partial removal of the coating was necessary to promote attractive interactions, unlike what was reported by Si *et al.*[13] However, it may prove useful for reducing defects, such as the coexistence of multiple ordered phases, as reported by Boles *et al.*[18]

This interdigitation of the alkyl chains is confirmed by the quantitative analysis of the SANS curve of OA-C18@CeO_2 250 sample (Fig. 7, and Table S7). The experimental data were fitted considering the presence of a face-centered cubic phase, yielding an inorganic core size of about 22 Å, which is consistent with TEM and DLS results, and an interparticle distance of about 35 Å, which is shorter than the combined length of two alkyl chains of oleylamine and oleic acid (approximately 50 Å). These findings suggest the interdigitation of the alkyl chains within the ordered aggregates.

Considering the interaction potential for two NPs in different systems and knowing how many pairs of NPs are present in two crystal structures, and therefore the number of interactions in the crystals, cell potentials were calculated. The potentials

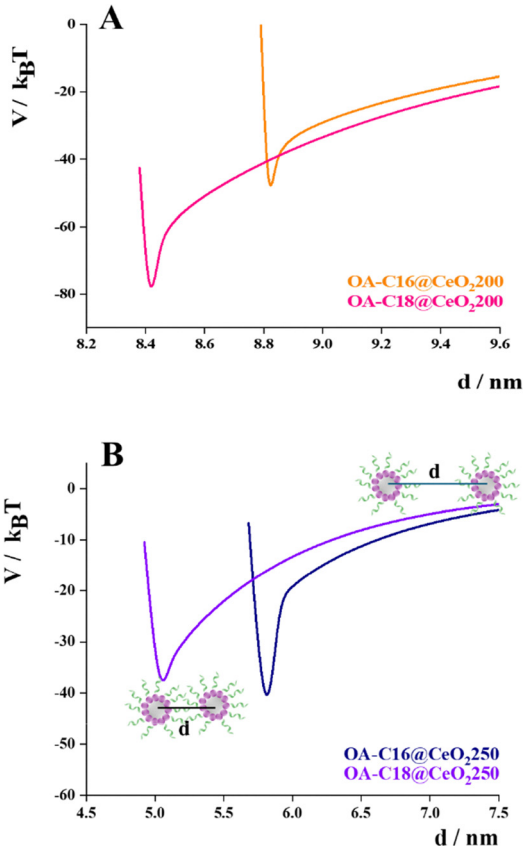

Fig. 6 Total interaction potential of OA-C16@CeO_2 200 (orange line), OA-C18@CeO_2 200 (pink line) (A), OA-C16@CeO_2 250 (blue line), and OA-C18@CeO_2 250 (violet line) (B).

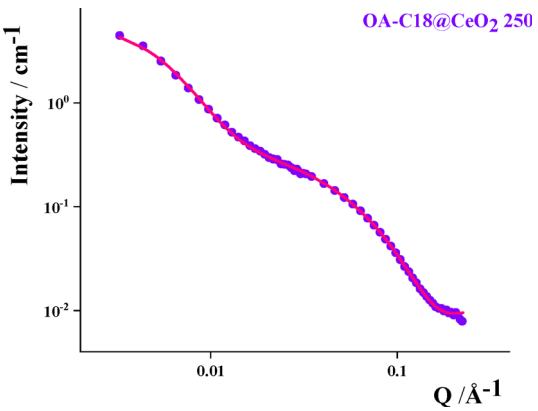

Fig. 7 SANS data (purple circles) and best fit curve (pink line) of OA-C18@CeO_2 250 sample in D_2O.

are equal to −6.8, −2.2, −5.8, and −5.4 kJ for OA-C16@CeO_2 200 (KF phase, 36 pair of NPs), OA-C18@CeO_2 200 (FCC phase, 7 pair of NPs), OA-C16@CeO_2 250 (KF phase, 36 pair of NPs), and OA-C18@CeO_2 250 (KF phase, 36 pair of NPs), respectively. There is an energy difference of about 3 kJ/k_BT between a face-centered cubic and a C14 Frank-Kasper phases, in agreement with that observed for an ordered hierarchical structure of gold nanoparticles.[26]

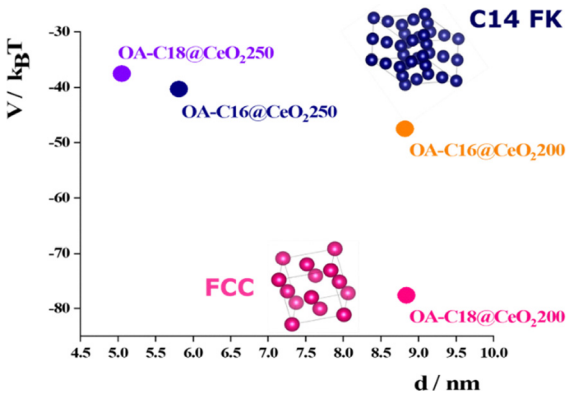

Fig. 8 Phase diagram.

The combination of all these results lead to create a diagram in which the interaction potential is plotted as a function of the distance between two neighboring nanoparticles (Fig. 8). It furnishes a direct picture how the geometric parameters influence the formation of disordered or ordered aggregates, confirming that nanoparticle self-aggregation is a complex process involving multiple factors. It is also interesting to note that all the systems whose predominant ordered phase is C14 FK exhibit interaction potentials ranged between −37 and −47 kJ/k_BT, whereas the only system that shows a deeper potential well displays a predominantly FCC-type structure.

3.3 OA-amine@CeO_2 NPs: investigating the optical properties of the superlattices

As previously demonstrated,[19] the induced ordered organization of coated CeO_2 NPs amplifies the optical properties if compared to disordered aggregates. On these bases, fluorescence spectroscopy measurements were carried out to understand how inducing a different organization of such NPs could be possible to modulate their emission properties. The fluorescence emission spectra obtained for the various superlattices suspended in water are shown in Fig. 9.

All the samples, upon excitation at 250 nm, show a broad emission (fluorescence) peak in the range 285–450 nm. However, qualitative and quantitative differences can be inferred from the comparison of the spectra. First, the area under each peak to evaluate the emission efficiency (*i.e.*, quantum yield) is calculated, as reported in Table 1. It is important to note that the spectra were collected using samples whose absorbances at the wavelength of excitation were similar (∼0.3), *i.e.*, the samples absorb the same number of photons (Fig. S10). Under these conditions, the area under the emission peak is directly proportional to the quantum yield of the NPs.[31] An inspection of Table 1 revealed that the disordered OA-C10@CeO_2 200 and OA-C12@CeO_2 200 show the lowest peak area, demonstrating that disordered structures are characterized by low fluorescence emission. Conversely, for the partially ordered OA-C16@CeO_2 200, a significant increase of the area under the peak was observed, *i.e.*, the sample is characterized by a higher quantum yield, now. The system OA-C18@CeO_2 200, which

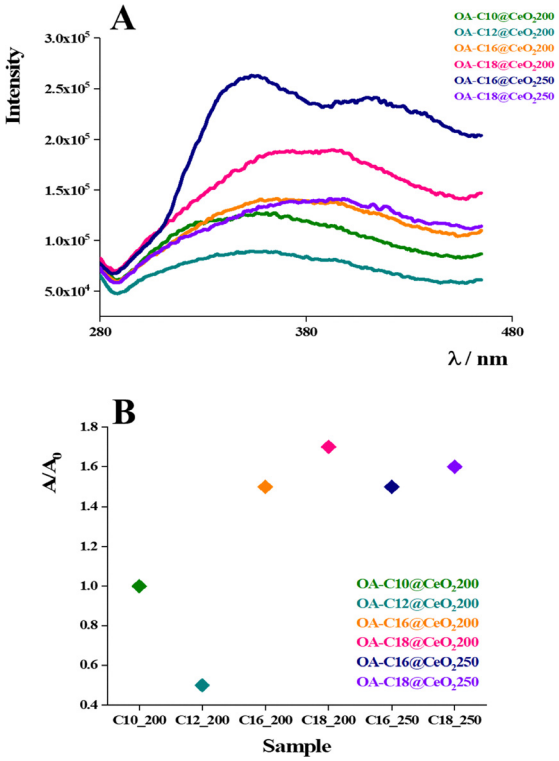

Fig. 9 Fluorescence spectra of OA-amine@CeO_2 NPs suspended in water, λ_{exc} = 250 nm (A), ratio between the area of each sample and the area of OA-C10@CeO_2 200.

Table 1 Integrated fluorescence intensity, and the ratio between the area of each sample and the area of OA-C10@CeO_2 200 (A_0)

Sample	Area/a.u. × 10^{-6}	A/A_0
OA-C10@CeO_2 200	6.38366 ± 0.00013	1
OA-C12@CeO_2 200	3.45723 ± 0.00009	0.5
OA-C16@CeO_2 200	9.2681 ± 0.0002	1.5
OA-C18@CeO_2 200	11.1065 ± 0.0003	1.7
OA-C16@CeO_2 250	9.6859 ± 0.0003	1.5
OA-C18@CeO_2 250	10.2927 ± 0.0003	1.6

presents a single ordered FCC phase, shows the highest area among the NPs produced at 200 °C. These data demonstrate that the degree of structural order and its relative amount are well correlated with the fluorescence quantum yield. It is interesting to note that the peak area for sample OA-C16@CeO_2 250 is similar to its counterpart produced at 200 °C. The two systems have the same predominant ordered phase, namely C14 FK. Finally, the OA-C18@CeO_2 250 showed a slightly lower peak area with respect to the same NPs produced at 200 °C. Probably, this is due to the presence of Frank-Kasper structure (together with FCC) observed for the OA-C18@CeO_2 250 NPs, which shows a lower quantum yield compared to FCC structures. In general, the highest quantum yield in the more ordered NPs can be due to the reduction of all non-radiative deactivation processes imposed by the structural organization and association among NPs,[21] which favors the radiative excited state deactivation pathway. From the emission spectra reported in Fig. 9,

other important features can be seen. All the samples show an emission band centered at around 315 nm. The emission spectra of ordered NPs are also characterized by an emission band at $\lambda > 350$ nm, which is absent in the two disordered systems (OA-C10@CeO_2 200 and OA-C12@CeO_2 200). The appearance of this last could be ascribable to the different interparticle distances imposed by the given structures. Indeed, changes in such parameters have been shown to be decisive in modulating the properties of other NP systems.[32] Thus, such a phenomenon may be also active in the present cases. Bearing in mind that for datasets acquired at different times, although using the same instrument, it is not possible to compare the intensity fluorescence values, we can nevertheless affirm that the data obtained are in agreement with what was previously observed.[21] Here, it is even more evident that by modulating the hierarchical organization, it is possible to tune the optical properties of CeO_2 NPs.

4. Conclusions

In this work, we demonstrate that the self-assembly and optical response of CeO_2 nanoparticles can be systematically controlled through the combined tuning of inorganic core dimensions and organic corona architecture. Amine@CeO_2 NPs are successfully synthesized through the thermal decomposition of cerium(III) nitrate hexahydrate, using as capping agents amines with different lengths of alkyl chains (from C8 to C18) and at three temperatures (150, 200, and 250 °C). The synthesis conditions leading to the formation of amine@CeO_2 NPs, whose characteristics are such that they can be functionalized, have been found to be high temperatures (200 and 250 °C) and long alkyl chains of organic coating (C16 and C18). Oleic acid (OA) functionalization highlights a clear correlation between nanoscale organization and photoluminescence behavior. Short-chain systems (C10 and C12) predominantly form disordered aggregates, resulting in reduced fluorescence intensity, whereas long-chain-coated nanoparticles assemble into well-defined superlattices. A reduction in the effective nanoparticle volume within the superlattice, driven by enhanced hydrophobic interparticle interactions, suppresses the presence of both disordered aggregates and isolated nanoparticles. Additionally, decreasing the inorganic core radius further promotes ordered packing, confirming the cooperative role of core size and surface chemistry in directing the assembly of amine@CeO_2 nanoparticles. The degree of structural order strongly influences the optical properties of the resulting assemblies. As the order degree in the system increases, the fluorescence intensity correspondingly rises. All the samples show an emission band centered at around 315 nm. However, the emission spectra of ordered NPs are also characterized by an emission band at $\lambda > 350$ nm, which is absent in the two disordered systems, and probably induced by the different interparticle distances imposed by the superlattice architecture.

Overall, these results highlight the key role of amphiphile-mediated strategy in driving the formation of 3D superstructures with advanced optical properties, opening to the development of increasingly well-organized nanosystems, thereby expanding the application potential of inorganic nanoparticles.

Author contributions

N. G. data curation, formal analysis, methodology, investigation, visualization, and writing the original draft; A. C. data curation, formal analysis, and writing – reviewing; R. O. data curation, formal analysis, and writing – reviewing; D. C. data curation, and formal analysis; R. D. G. data curation, formal analysis, and writing – reviewing; N. C. investigation, validation, and writing – reviewing; G. V. methodology, supervision, and writing – reviewing; L. P. conceptualization, funding acquisition, project administration, resource, supervision, writing – reviewing, and editing.

Conflicts of interest

There are no conflicts to declare.

Data availability

The data supporting this article have been included in the manuscript and as part of the supplementary information (SI). The raw data is available from the corresponding author upon reasonable request. The SI contains the following information: synthesis conditions, TEM images, size distribution histograms, hydrodynamic radius distribution, IR spectra, TGA curves, XRD spectra, SAXS patterns, equations of interaction potentials, and UV-Vis spectra. See DOI: https://doi.org/10.1039/d5tc03467a.

Acknowledgements

This project has received funding from the European Union's Horizon 2020 research and innovation program under grant agreement No. 101007417 having benefitted from the access provided by the Jülich Centre for Neutron Science at the Meier Leibnitz Zentrum in Garching bei München, Germany within the framework of the NFFA-Europe Pilot Transnational Access Activity (nffa.eu), proposal ID677. Work supported by the National Recovery and Resilience Plan (NRRP), Mission 4, Component 2, Investment 1.5, The Tuscany Health Ecosystem – THE (project no. ECS00000017) – Spoke 8 – Biotechnologies And Imaging In Neuroscience, Project ''Nanosonde per la diagnosi da retina di malattie neurodegenerative – NANOEYE'', CUP: E67G24000380006, funded by the European Union – NextGenerationEU.

References

1 S. Rajeshkumar and P. Naik, *Biotechnol. Rep.*, 2018, **17**, 1.
2 R. Fiorenza, L. Spitaleri, A. Gulino and S. Scirè, *Catalysts*, 2018, **8**, 203.
3 H. Liu, A. Bright, M. N. Stephane, F. M. Elvira, R. Anaman, H. Chen, K. Xiang and J. Wu, *Surf. Interfaces*, 2025, **72**, 107219.

4 C. Maria Magdalane, K. Kaviyarasu, A. Raja, M. V. Arularasu, G. T. Mola, A. B. Isaev, N. A. Al-Dhabi, M. V. Arasu, B. Jeyaraj, J. Kennedy and M. Maaza, *J. Photochem. Photobiol., B*, 2018, **185**, 275.
5 J. A. Rodriguez, D. C. Grinter, Z. Liu, R. M. Palomino and S. D. Senanayake, *Chem. Soc. Rev.*, 2017, **46**, 1824.
6 M. Gu, W. Li, L. Jiang and X. Li, *Acta Biomater.*, 2022, **148**, 22.
7 P. Jethva, M. Momin, T. Khan and A. Omri, *Materials*, 2022, **15**, 2374.
8 J. Wu, X. Wang, Q. Wang, Z. Lou, S. Li, Y. Zhu, L. Qin and H. Wei, *Chem. Soc. Rev.*, 2019, **48**, 1004.
9 A. Dhall and W. Self, *Antioxidants*, 2018, **7**, 97.
10 Z. Lu and Y. Yin, *Chem. Soc. Rev.*, 2012, **41**, 6874.
11 J. K. Stolarczyk, A. Deak and D. F. Brougham, *Adv. Mater.*, 2016, **28**, 5400.
12 N. S. Mueller, E. Pfitzner, Y. Okamura, G. Gordeev, P. Kusch, H. Lange, J. Heberle, F. Schulz and S. Reich, *ACS Nano*, 2021, **15**, 5523.
13 K. J. Si, Y. Chen, Q. Shi and W. Cheng, *Adv. Sci.*, 2018, **5**, 1700179.
14 X. Bouju, É. Duguet, F. Gauffre, C. R. Henry, M. L. Kahn, P. Mélinon and S. Ravaine, *Adv. Mater.*, 2018, **30**, 1706558.
15 B. Pansu, C. Goldmann, D. Constantin, M. Impéror-Clerc and J.-F. Sadoc, *Soft Matter*, 2021, **17**, 6461.
16 K. Bian, H. Schunk, D. Ye, A. Hwang, T. S. Luk, R. Li, Z. Wang and H. Fan, *Nat. Commun.*, 2018, **9**, 2365.
17 J. J. Calvin, A. S. Brewer and A. P. Alivisatos, *Nat. Synth.*, 2022, **1**, 127.
18 M. A. Boles, M. Engel and D. V. Talapin, *Chem. Rev.*, 2016, **116**, 11220.
19 S. S. Lee, W. Song, M. Cho, H. L. Puppala, P. Nguyen, H. Zhu, L. Segatori and V. L. Colvin, *ACS Nano*, 2013, **7**, 9693.
20 N. Gallucci, G. Vitiello, R. Di Girolamo, P. Imbimbo, D. M. Monti, O. Tarallo, A. Vergara, I. Russo Krauss and L. Paduano, *Nanomaterials*, 2021, **11**, 542.
21 N. Gallucci, M.-S. Appavou, N. Cowieson, G. D'Errico, R. Di Girolamo, S. Lettieri, F. Sica, G. Vitiello and L. Paduano, *J. Colloid Interface Sci.*, 2024, **659**, 926.
22 N. Gallucci, M. Hmoudah, E. Martinez, A. El-Qanni, M. Di Serio, L. Paduano, G. Vitiello and V. Russo, *J. Environ. Chem. Eng.*, 2022, **10**, 107866.
23 N. P. Cowieson, C. J. C. Edwards-Gayle, K. Inoue, N. S. Khunti, J. Doutch, E. Williams, S. Daniels, G. Preece, N. A. Krumpa, J. P. Sutter, M. D. Tully, N. J. Terrill and R. P. Rambo, *J. Synchrotron Radiat.*, 2020, **27**, 1438.
24 A. Cangiano, N. Gallucci, A. Giarra, J. Ali, L. Chiappisi, N. P. Cowieson and L. Paduano, *Nanoscale*, 2025, **17**, 15829.
25 F. Vratny, S. Kern and F. Gugliotta, *J. Inorg. Nucl. Chem.*, 1961, **17**, 281.
26 S. S. Lee, H. Zhu, E. Q. Contreras, A. Prakash, H. L. Puppala and V. L. Colvin, *Chem. Mater.*, 2012, **24**, 424.
27 P. R. A. F. Garcia, O. Prymak, V. Grasmik, K. Pappert, W. Wlysses, L. Otubo, M. Epple and C. L. P. Oliveira, *Nanoscale Adv.*, 2020, **2**, 225.
28 H. Noh, S. F. Liew, V. Saranathan, S. G. J. Mochrie, R. O. Prum, E. R. Dufresne and H. Cao, *Adv. Mater.*, 2010, **22**, 2871.
29 S. Hajiw, B. Pansu and J.-F. Sadoc, *ACS Nano*, 2015, **9**, 8116.
30 S. N. Lysenko, S. A. Astaf'eva, E. V. Kornilitsina, D. E. Yakusheva and K. I. Morozov, *Langmuir*, 2022, **38**, 14313.
31 B. Valeur and M. N. Berberan-Santos, *Molecular fluorescence: principles and applications*, John Wiley & Sons, 2013.
32 K. L. Young, M. B. Ross, M. G. Blaber, M. Rycenga, M. R. Jones, C. Zhang, A. J. Senesi, B. Lee, G. C. Schatz and C. A. Mirkin, *Adv. Mater.*, 2014, **26**, 653.